

Contents

Supplementary Figures	2
Fig. S1. Generation of a novel transgene for the oscillating gene <i>her1</i>	3
Fig. S2. Characterization of morphological segmentation in <i>Looping</i>	4
Fig. S3. Comparison of YFP intensity kymographs and phase maps	5
Fig. S4. The number of kinematic waves of oscillating genes decrease during segmentation	6
Fig. S5. Kymographs of the average phase map and phase profile	7
Fig. S6. Kymographs of wavelengths and frequencies of the average phase map	8
Fig. S7. Time dependence of different frequency components	9
Fig. S8. Time dependence of fit parameters	10
Supplementary Movie legends	11
Materials and methods	12
BAC recombineering and zebrafish transgenesis	12
Fish care and imaging preparation	12
Time-lapse imaging and temperature control	13
Image processing	13
Period measurements and statistics	13
Whole-mount in situ hybridizations and static images	14
Supplementary Text	15
Generating phase maps with a wavelet transform	15
Representation of oscillatory time series in terms of phase and amplitude	15
Wavelet transform	15
Phase maps	16
Doppler effect and dynamic wavelength effect	17
Contributions to the frequency offset	17
Discussion of simple scenarios	18
Quantification of Doppler effect and dynamic wavelength effect in experiments	20
Supplementary Tables	22
Table S1. Fit functions used in the Supplementary Text	22
Table S2. Numerical values of the fit parameters of the functions given in Table S1	23

Supplementary Figures

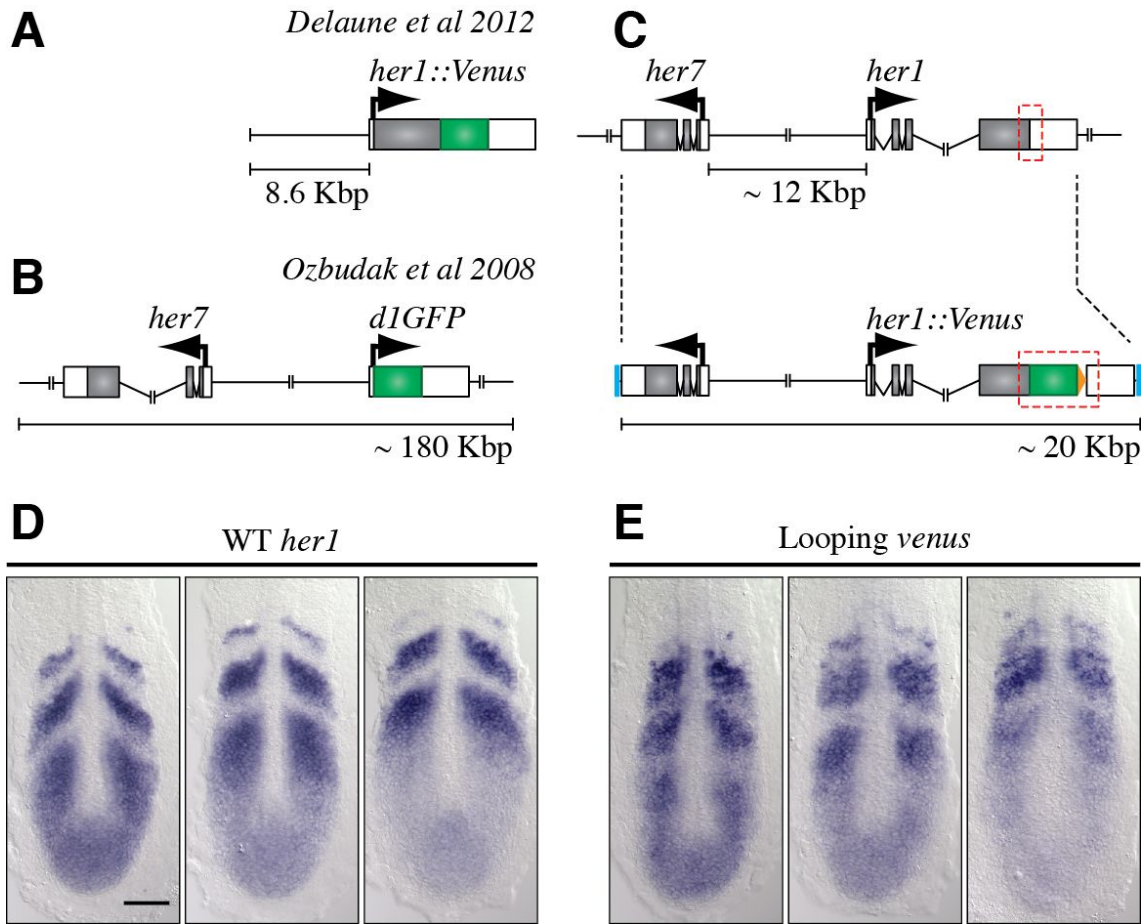


Figure S1 Generation of a novel transgene for the oscillating gene *her1*. (A–C) Comparison with state-of-the-art transgene constructs designed to visualize *her1* oscillations in vivo. (A) Delaune et al., 2012 (2) fused the coding region of *her1* (gray box) and Venus (green box) and ligated this reporter fusion gene to a sub-fragment of the *her1* and *her7* intergenic region (8.6 Kbp) and the 3' UTR of *her1* (white box). The resulting reporter transgene mimics oscillatory behavior at the mRNA and protein level only in the anterior and intermediate PSM and suffers from ectopic reporter expression in the notochord (2). (B) Ozbudak et al., 2008 (14) employed BAC recombineering to replace the coding region of *her1* with d1GFP. This construct mimicked mRNA oscillations but the fluorophore d1GFP was insufficiently destabilized to mimic protein oscillations. (C) In this study, BAC recombineering was used to embed the coding sequence of Venus into the intact chromosomal locus of *her1*. This strategy yielded a Her1::Venus fusion protein and aimed to exploit all regulatory cues harbored in the endogenous locus. In a second recombination step this minimally modified locus was subcloned into a plasmid backbone containing *I-SceI* Meganuclease sites (blue). (D,E) Comparison of endogenous and transgene mRNA patterns in flat-mounted wildtype and *Looping* siblings at 12 somites. (D) Expression patterns for the endogenous oscillating gene *her1* are very dynamic and reminiscent of waves traveling across the pre-somitic mesoderm (PSM). (E) The reporter mRNA in *Looping* siblings mimics this oscillatory behavior in the entire PSM. Anterior to the top, Scale bar = 100 μ m. Kbp = Kilo base pair

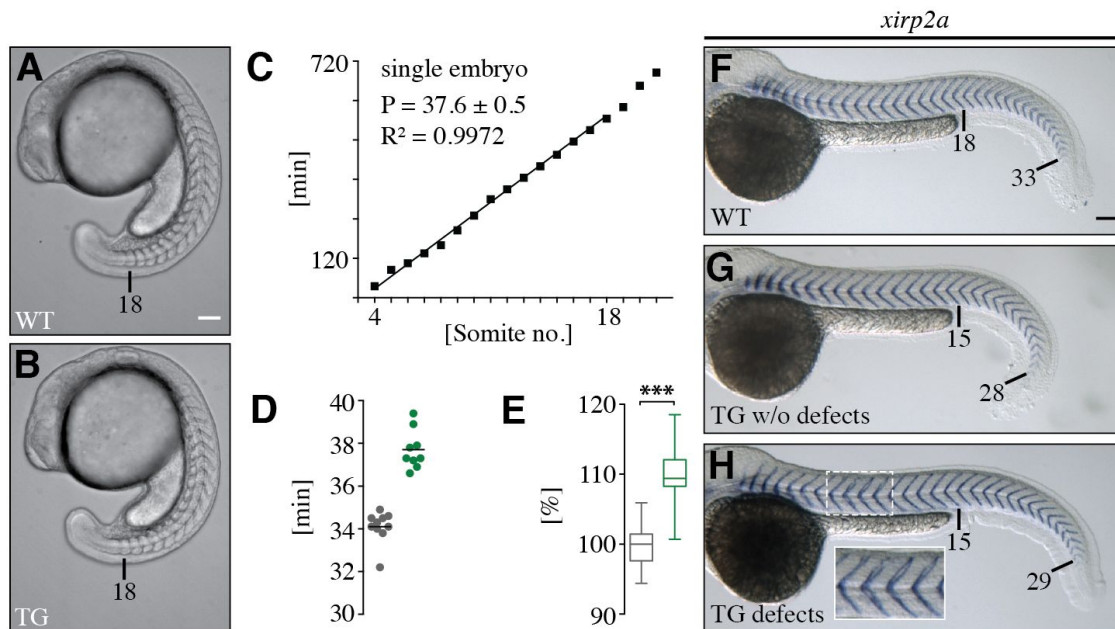


Figure S2 Characterization of morphological segmentation in *Looping*. (A, B) Visually there is no difference in segment formation between Wildtype (WT) and *Looping* (TG) siblings. (C–E) Comparison of segmentation periods in wildtype (gray) and *Looping* (green) siblings. (C) The formation of somites/segments is scored visually and the segmentation period of individual embryos is calculated from a linear regression. The latter is limited to trunk segmentation, which is known to happen with a constant period (13). (D) Dot plot of wildtype (gray, $n = 10$) and *Looping* (green, $n = 9$) segmentation periods: A single time-lapse experiments reveals that the mean segmentation period (black bar) is different in wildtype and *Looping* siblings. (E) Box and Whisker plot of wildtype (gray, $n = 38$) and *Looping* (green, $n = 40$) segmentation periods: Segmentation periods were normalized to the mean wildtype period in each experiment and pooled subsequently. *Looping* siblings segment on average 10% slower than their wildtype siblings (Whiskers min/max, *** $p < 0.0001$, $N = 4$, $n = 40$). (F–H) In situ hybridizations against *xirp2a* mark segment boundaries and are used to compare segment morphology in wildtype and *Looping* littermates. (F) The ‘chevron’ shape and the total number of segments are key features in wildtype animals. (G) In 53% (35/66) of *Looping* animals this morphology is unchanged. (H) In 47% (31/66) of *Looping* siblings minor segment defects occur (inset H), however the overall chevron shape is unaffected. Consistent with the measured period change, the total number of segments is reduced in *Looping* siblings (compare F–H). Scale bars = 100 μm , Numbers in (A,B,F–H) indicate somite/segment number

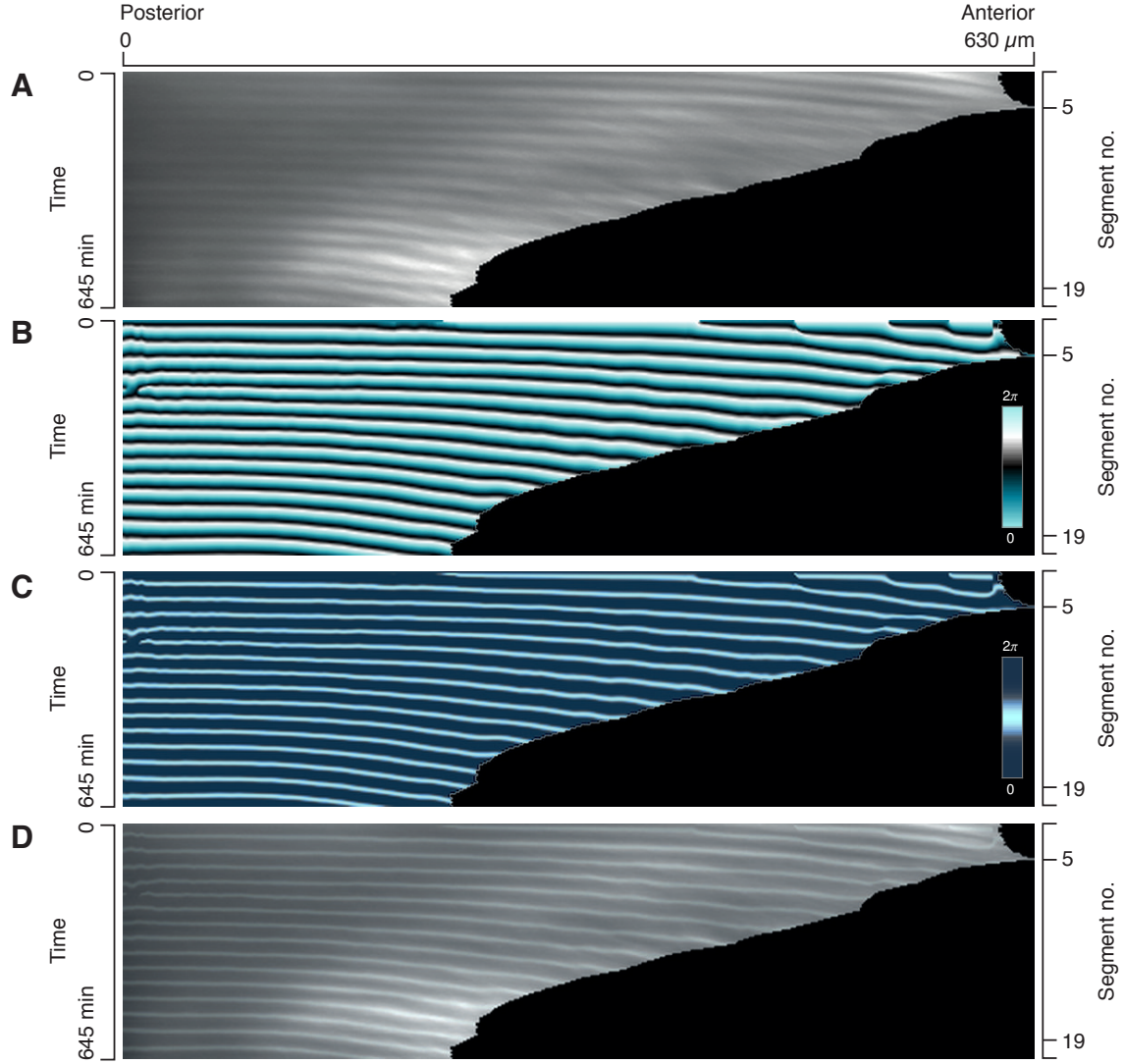


Figure S3 Comparison of YFP intensity kymographs and phase maps. (A) YFP intensity kymograph from Fig. 2A of the main text. (B) Corresponding phase map from Fig. 2C of the main text. (C) Phase map using a different color code for visual clarity of the overlay in D. (D) The overlay of the intensity kymograph A and the phase map C shows that the phase maps accurately capture the spatio-temporal features of oscillations in the PSM.

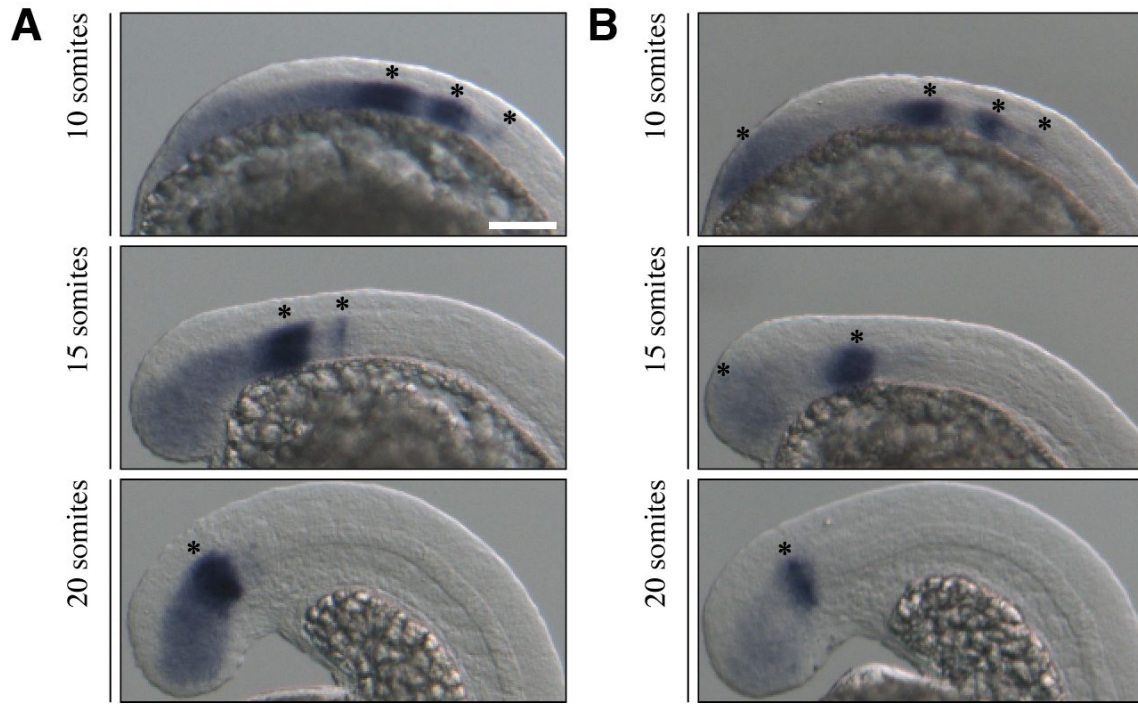


Figure S4 The number of kinematic waves of oscillating genes decrease during segmentation. (A) In situ hybridization of mRNA from the oscillating gene *her1* in wildtype embryos. Individual snapshots of the endogenous mRNA pattern show firstly that the length of the oscillating tissue decreases during segmentation, and also reveal the pattern of endogenous oscillating gene expression. Expression domains are reminiscent of waves that travel through the PSM. The number of these waves (asterisks) visible in the tissue decreases as somites/segments are sequentially formed. Scale bar = 100 μ m, posterior PSM to the top left (B) Time series of in situ hybridization against mRNA of the oscillating gene *her7* in wildtype embryos. A decrease of number of kinematic waves is a shared feature of oscillating genes in the segmenting zebrafish PSM.

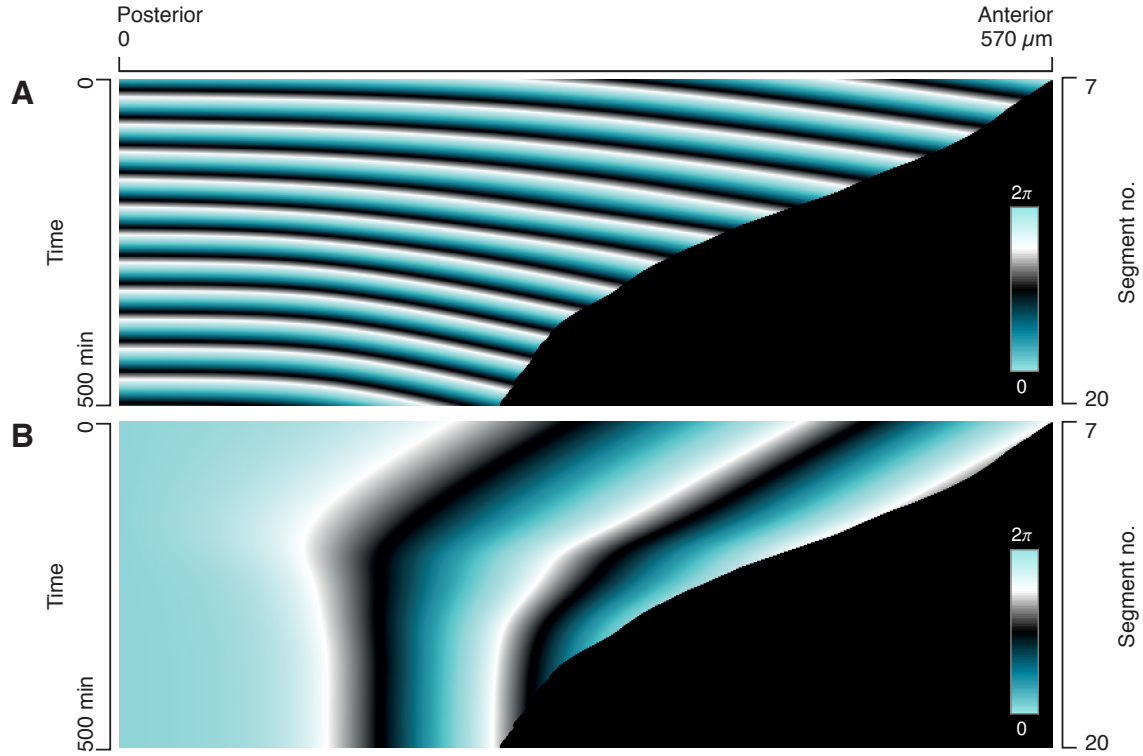


Figure S5 Kymographs of the average phase map and phase profile. (A) The average phase map $\Phi(x, t)$ describing spatio-temporal wave patterns. **(B)** The average phase profile $\Psi(x, t) = \Phi(x, t) - \Phi(0, t)$. Over the time range of 500 min, one kinematic wave (a phase increment of 2π along the PSM) is removed from the PSM due to tissue shrinking. See Supplementary Text for details. The color code is the same as in Fig. 2C of the main text.

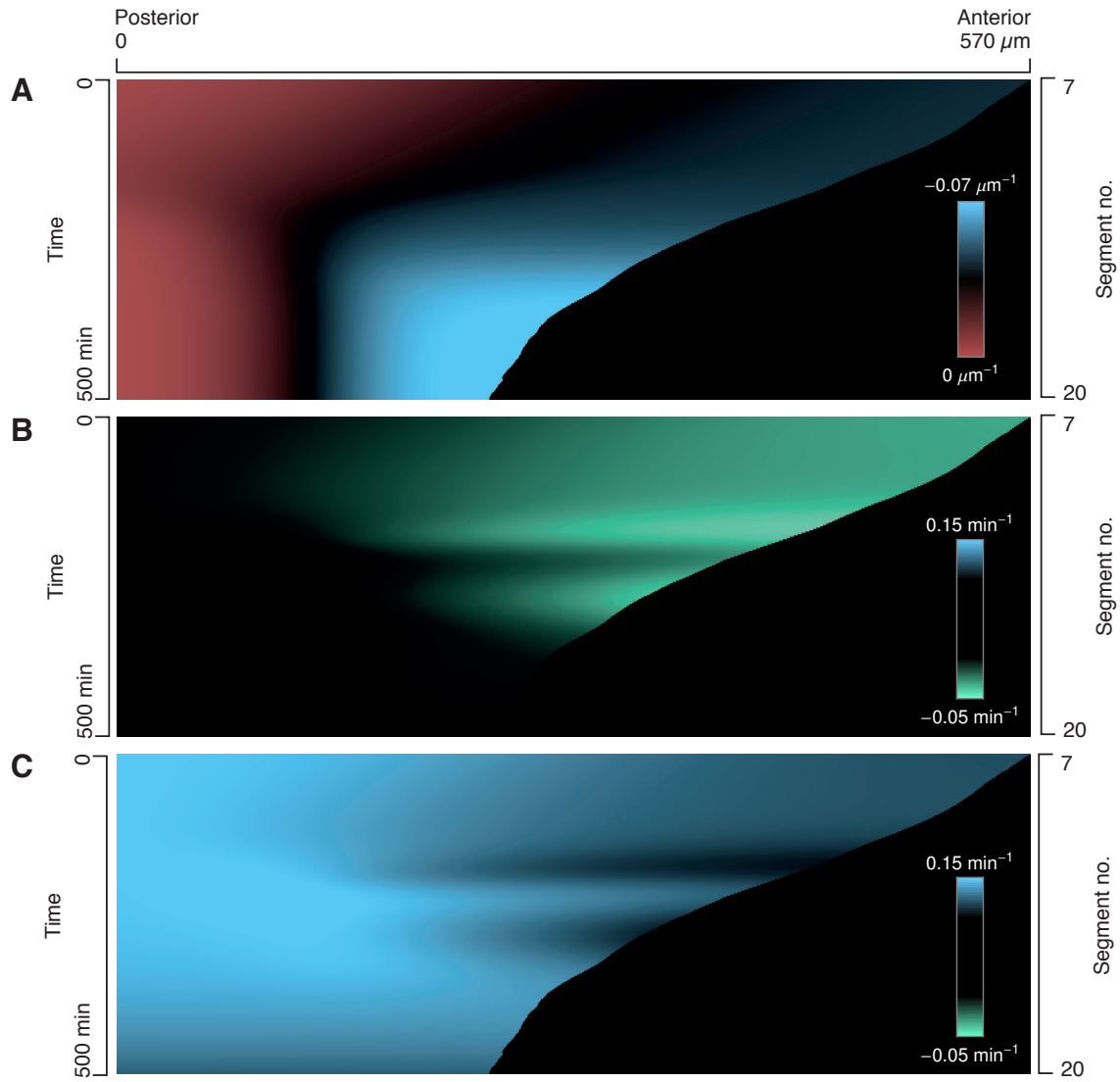


Figure S6 Kymographs of wavelengths and frequencies of the average phase map. (A) Inverse wavelength $\partial\Psi/\partial x$ of the average phase profile $\Psi(x, t)$. **(B)** Rate of change $\partial\Psi/\partial t$ of the average phase profile $\Psi(x, t)$. **(C)** Local frequency $\partial\Phi/\partial t$ of the average phase map $\Phi(x, t)$. See Supplementary Text for details.

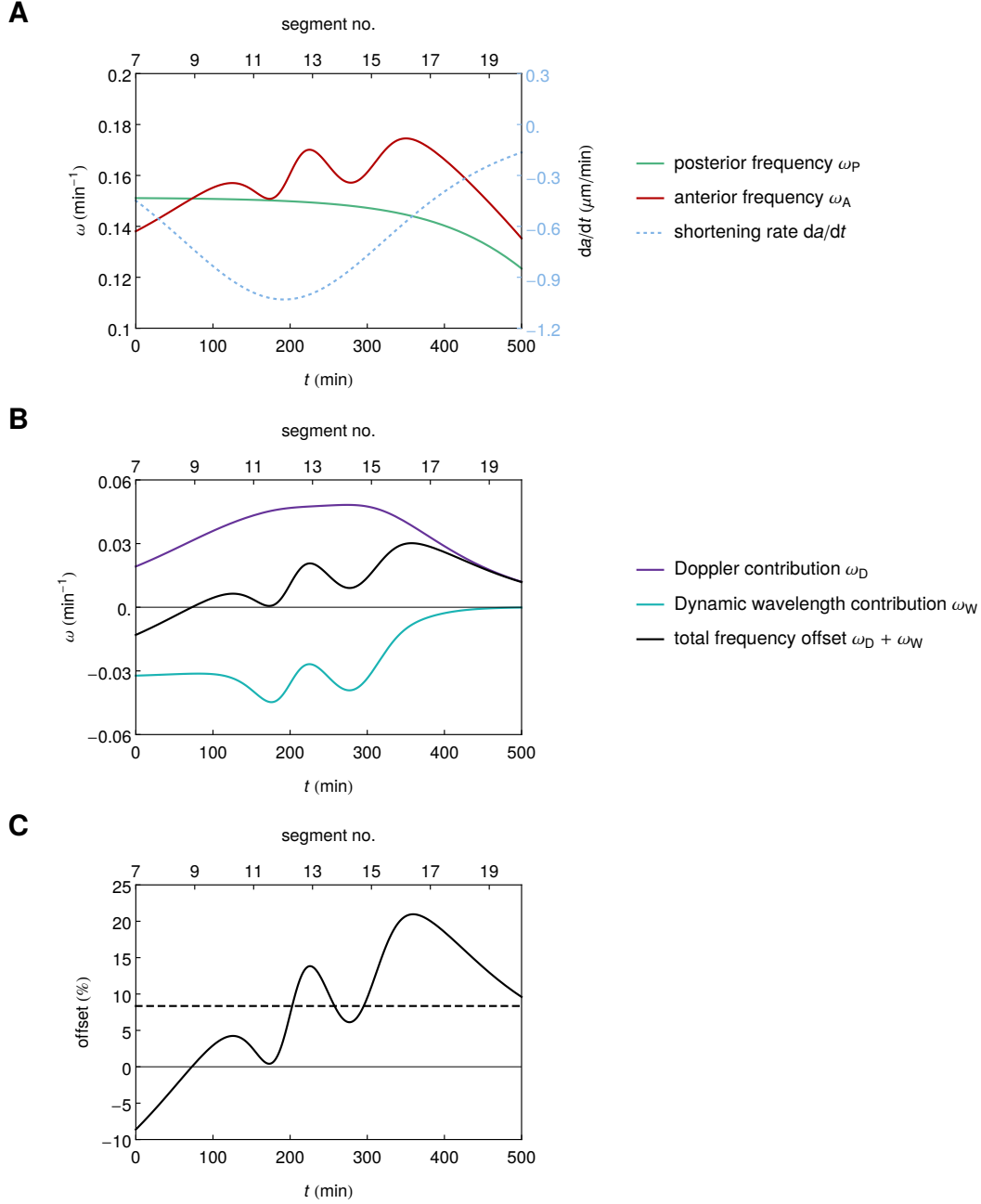


Figure S7 Time dependence of different frequency components. (A) Posterior frequency ω_P (green), anterior frequency ω_A (red), and the PSM shortening rate da/dt (dotted blue) as a function of time. **(B)** Contributions ω_D (purple) and ω_W (cyan) to the frequency offset $\omega_A - \omega_P = \omega_D + \omega_W$ (black). **(C)** The relative offset $(\omega_A - \omega_P)/\omega_P$ (solid black) between anterior and posterior frequency shown in A. The temporal average is shown by a dashed line. All frequencies are determined from the average phase map $\Phi(x, t)$, see Supplementary Text for details.

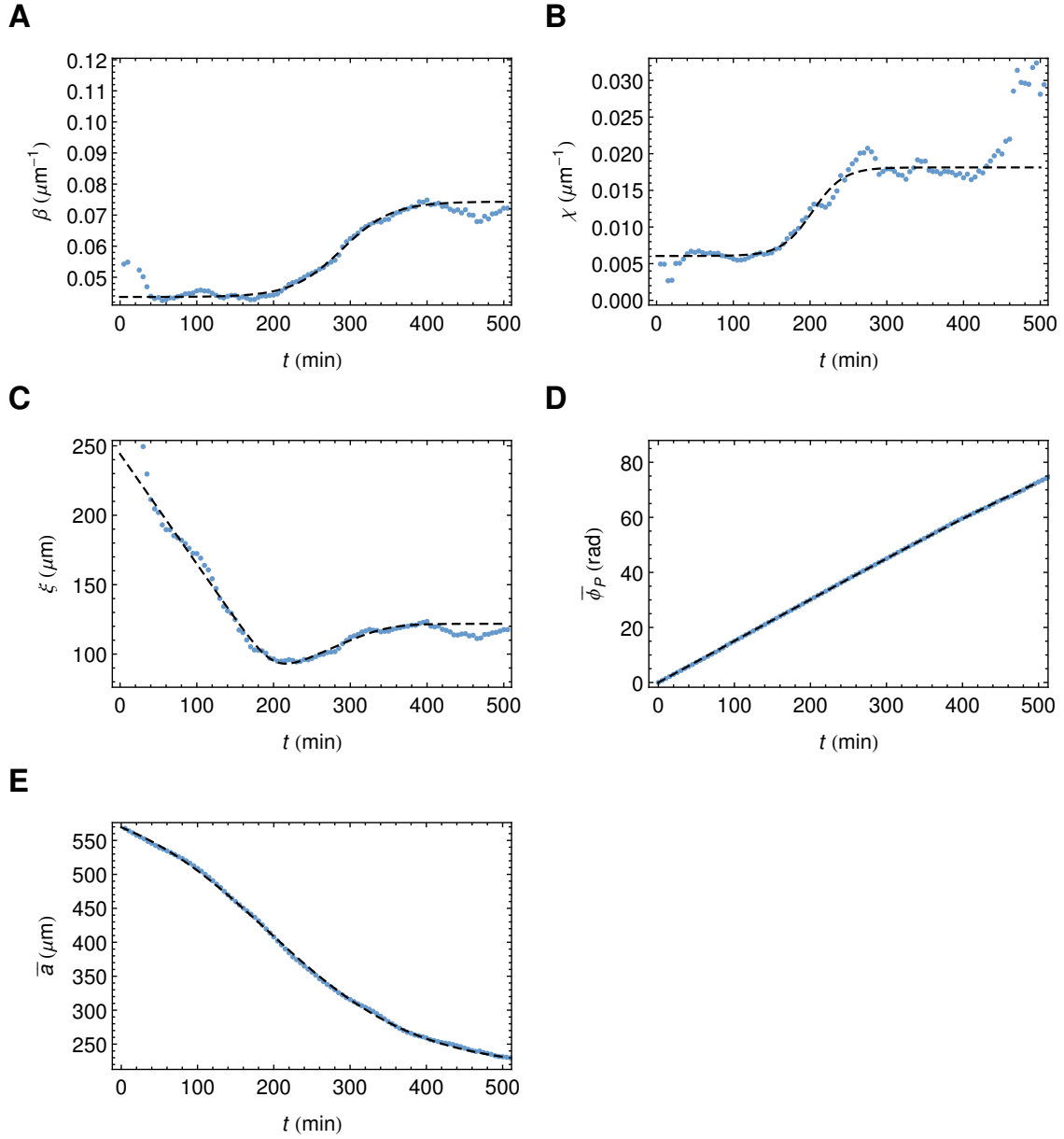


Figure S8 Time dependence of fit parameters. (A–C) The values of the coefficients β , χ , and ξ parameterizing the phase profile $\Theta(x)$ (see Table S1) obtained by fits at each time point (blue). These data are fit by the functions f_β (A), f_χ (B), and f_ξ (C) (black dashed). (D) Average posterior phase $\bar{\phi}_P$ determined at individual time points (blue), together with the fit to the function $\Phi_P(t)$ (black dashed) (see Table S1). (E) Average PSM length \bar{a} determined at individual time points (blue), together with the fit to the function $A(t)$ (black dashed) (see Table S1). Fit parameter values are provided in Table S2.

Supplementary Movie legends

Movie S1: Real-time imaging of segment formation and Her1::Venus oscillations during segmentation in transgenic *Looping* embryos

This movie shows representative brightfield and YFP channels for 1 position of a multidimensional time-lapse after z-stack projection. The brightfield channel illustrates that the unsegmented pre-somitic mesoderm (PSM) is sequentially subdivided into precursors of adult segments, the somites. The YFP channel shows that the morphologically unsegmented tissue exhibits patterns of oscillating gene expression that are reminiscent of waves that travel from the posterior to the anterior where they arrest. Phenomena in both channels happen with a specific rhythmicity and directionality.

Movie S2: Overlay of brightfield and fluorescence channels during segmentation in transgenic *Looping* embryos

Overlay of brightfield and YFP channels indicates that new segment boundaries form when kinematic waves arrest in the anterior PSM. 16 color LUT (blue, lowest and red highest intensity).

Movie S3: Comparison of kinematic waves in the YFP channel and the phase map

Upper panel shows the YFP fluorescence channel cropped and straightened from the tailbud and PSM of a representative *Looping her1-YFP* transgenic embryo during the formation of somites 2 to 20. Lower panel shows the corresponding horizontal lines of the phase map described in quantitative methods section (PQR).

Movie S4: Time evolution of the phase profiles from population of *Looping her1-YFP* zebrafish embryos

Phase profiles from across the tailbud and PSM of 18 embryos are shown in a range of blue changing from 7 to 20 somites. Note the decreasing PSM length along the x -axis and the decrease in total phase offset on the y -axis during the developmental time interval.

Movie S5: Time evolution of the median phase profile and the spatio-temporal fit

Median of all phase profiles (solid blue curve) from Supplementary Movie S4 and the spatio-temporal fit introduced in the Supplementary Text (dashed green curve).

Materials and methods

BAC recombineering and zebrafish transgenesis

Two successive rounds of BAC recombineering were used as described previously (15, 16) to (1) create a functional fusion between the coding regions of *her1* and Venus and to (2) subclone the modified chromosomal locus into a plasmid backbone. The latter served to restrict the size of the modified BAC and introduce two *I-SceI* Meganuclease sites, which aimed for high transgenesis frequencies (17). The following homology arms were used for tagging:

L: 5'–GGACTCTGAGACGAGCGCTGTTCCACAATCAGCCTTTGTGGAGACCCTGG–3'

R: 5'–CCCTTTAAGACAACGCTGGTTATTCTCATGCTAAGTGTCTTCAGTTTTGC–3'

and for subcloning

L: 5'–GTTATGTGTTCCCGACAATAATATTAATCTCTGGAGTGGCATGATGTTTG–3'

R: 5'–TGCTTTTTGTATGACTCGTTTCTTTACATTTGGGCTTAAATAAATAGATT–3'.

The resulting construct was co-injected with *I-SceI* Meganuclease (Roche) at a DNA concentration of 100 ng/μl and a bolus size of 100 μm as described previously (18). *I-SceI* Meganuclease transgenesis was used to generate a pool of independent transgenic founders with single, low-copy insertions into the host genome (17). This feature allows the reporter expression levels to be tuned without altering the stability of the reporter protein itself and was used to find the right balance between reporter stability and sensitivity of the imaging set-up. Transient transgenic expression was assessed to verify the functionality of the YFP fusion but ignored as selection criterion for putative transgenic founders. All injected embryos without obvious phenotype were raised to sexual maturity to avoid any visual bias towards strongly expressing founder. Initially, putative transgenic founders were screened by visual inspection of their F1 progeny after outcrossing to WT animals with a common stereomicroscope (Olympus, SZX-16) equipped with an appropriate filter set (AHF, YFP) and light source (Lumen dynamics, X-cite 120). Based on this conventional approach, only 1 transgenic founder could be isolated. Therefore, the screening assay was changed to increase sensitivity levels and whole-mount in situ hybridization was used to isolate 4 more transgenic founders that were positive for YFP/Venus mRNA. In total, 5 independent transgenic founders were identified from a single injection experiment, yielding an average transgenesis frequency of ~25% and transmission frequencies below 50%. Reporter expression was qualitatively similar but quantitatively different for all isolated transgenic founders. Based on the optimal signal to noise ratio, one founder was selected for time-lapse experiments and named *Looping*. This transgenic line is viable and fertile and continues to stably express Venus after seven generations.

Fish care and imaging preparation

Wildtype (WT) AB and transgenic fish were maintained according to standard procedures. All analyzed embryos were obtained from outcrosses of heterozygous *Looping* animals to WT fish by natural spawning. Embryos were collected within 15 minutes after spawning to minimize asynchronous clutches/siblings and incubated in E3 without methylene blue at all times. For imaging experiments, embryos were collected and incubated at 33°C till bud stage, de-chorionated and allowed to equilibrate at room temperature. Prior to imaging, 10 wildtype and 10 transgenic siblings

were randomly distributed and laterally aligned in conical depressions in a pad of agarose (Sigma, low-melting, 2% in E3) that was cast in a glass-bottom dish (Matek, 35 mm). The size of these conical depressions was chosen to fit only the yolk of an embryo. Consequently, embryos could grow without physical restrictions on top of the agarose pad and were stabilized in *z*-direction. The imaging dish contained E3 with 0.014% Tricaine to prevent muscle twitching and was allowed to equilibrate at least 30 minutes in the thermal insert of the time-lapse set-up prior imaging was started.

Time-lapse imaging and temperature control

A wide-field microscope (Zeiss, Axiovert 200M) equipped with a 10X objective (Zeiss, NA 0.5), an automated stage (Maerzhaeuser), a LED-based light source (Lumencor, SpectraX7), an EM-CCD camera (Andor, iXon 888) and a thermal insert (Harvard apparatus) was used to record zebrafish segmentation in 2 channels, 6 *z*-slices (range: 100 μm in 20 μm steps) for 20 *xy*-positions at an time interval of 5 minutes for at least 12 hours. To balance imaging parameters and sampling rate during recordings, we chose 23.5°C as experimental temperature, which was close to room temperature and facilitated temperature control. During each experiment the temperature was controlled by the closed thermal insert and monitored by an independent external thermometer that was used to log temperatures throughout recordings, which typically ranged between 23.3°C to 23.6°C. To compare measurements from different experiments/days at slightly different temperatures, we included 10 WT siblings in each experiment that were used to normalize the measured somitogenesis period. The random distribution of wildtype and transgenic siblings in the imaging dish avoided any bias due to temperature gradients within the imaging dish.

Image processing

All image processing was carried out using the open-source Fiji distribution of ImageJ (19) and all tools developed for this manuscript are available at <http://fiji.sc/Fiji>. A novel stack focusing technique was developed inspired by Bayesian inference to extract in-focus, single layer images from brightfield *z*-stacks containing 6 images at several focal depths (“Gaussian StackFocusing”). YFP *z*-stacks were objected to maximum projections. To facilitate analyzing the reporter intensity in a population of zebrafish embryos, we developed interpolator tools to locally (“ROI/Circle Interpolator”) or globally (“LOI Interpolator”) measure the average reporter intensity within the PSM. All measurements were performed on *z*-projections without any further image processing. The ROI area was set constantly to a diameter of 40 pixel, the LOI width to 30 pixel. For illustration purposes only, all images and movies in this manuscript have been subjected to a Gaussian blur with a radius of 1×1 . Overlays of brightfield and YFP channels were done using the “Compose RGB-Stack” plug-in available in Fiji.

Period measurements and statistics

All period measurements were restricted to trunk segmentation, because the segmentation period was shown to be constant over this developmental interval (13). The formation of segments was scored visually as described previously (13). Shortly, the first visible sign of each somite boundary was determined and each successive time point was noted. For each embryo we plotted the

number of somites over time and calculated the average segmentation period from a linear regression through these data points (Fig. S2). These individual period measurements were pooled according to their genotype and used to calculate the mean segmentation period for a given experiment. The average segmentation period of WT siblings was set to 100% and used to normalize all other period measurements for a given experiment. The periods of genetic oscillations were determined locally using the ROI interpolator tool available in Fiji. The obtained raw traces (mean gray values over time) were exported to Prism 6 and analyzed using the standard function for the second derivative. The average period per embryo was calculated from the interpeak distance of the resulting curves. As above, individual periods were pooled to obtain an average period for oscillations in the anterior and posterior for a give experiment. The period offset between anterior and posterior oscillations was significant ($p < 0.001$) in all 4 independent experiments. The period of segment formation and anterior oscillations was never significantly different. To calculate the average period offset between segmentation, anterior and posterior oscillations, we pooled all period measurements from 4 experiments after normalization. All unpaired t-test were calculated using Prism 6 assuming normal distribution and Welch-correction.

Whole-mount in situ hybridizations and static images

In situ hybridization and riboprobe generation was performed as described (24, 25, 26). Whole-mount in situ hybridizations were documented with a stereomicroscope (Olympus, SZX-12) equipped with an appropriate CCD camera (Qimaging, Micropublisher). Flat-mounted embryos were photographed using an Axioskop 2 equipped with a RGB camera (QImaging, Retiga SRV).

Supplementary Text

Generating phase maps with a wavelet transform

In this section, we explain how oscillatory time series can be represented in terms of phase and amplitude. We then show how to obtain a phase representation of an oscillatory signal using a wavelet transform and apply this technique to the experimentally obtained intensity kymographs. We use this phase representation (i) to systematically measure the number of kinematic waves in the PSM, (ii) to directly compare the spatio-temporal features of wave patterns across a population of different embryos, and (iii) to quantify the magnitude of the Doppler effect and the dynamic wavelength effect (see main text) from experimental data.

Representation of oscillatory time series in terms of phase and amplitude

Consider an oscillatory signal of the type

$$Q(t) = q_0 + q(t) \cos \phi(t) , \quad (\text{S1})$$

where q_0 is a constant, $q(t)$ is the amplitude of oscillations and $\phi(t)$ is the phase. For a constant amplitude, $q(t) = \bar{q}$, and a linearly increasing phase, $\phi(t) = \omega t$, this signal oscillates with an angular frequency ω , corresponding to a period of $T = 2\pi/\omega$. The phase $\phi(t)$ thus represents the progress in the oscillation cycle at time t .

In general, every signal $Q(t)$ that exhibits fairly regular oscillations can be expressed in a way similar to Eq. (S1). The representation of $Q(t)$ in terms of an amplitude $q(t)$ and a phase $\phi(t)$ is however not unique but based on a separation of time scales. The phase $\phi(t)$ captures the features of $Q(t)$ on the time scale of the period of oscillations, while $q(t)$ captures amplitude variations on slower time scales. Moreover, since $\cos \phi$ is 2π -periodic in ϕ , the signal $Q(t)$ does not change if we replace ϕ by $\varphi = \phi \bmod 2\pi$, that is, by a phase φ that evolves in the same way as ϕ except that it is reset to 0 whenever it reaches 2π .

A method to systematically obtain a phase signal $\varphi(t)$ from a time series $Q(t)$ is the so-called wavelet transform (22), presented in the next section. It explicitly keeps track of the ambiguities in the definition of the phase and allows to systematically address them.

Wavelet transform

We consider a discrete time series $Q = (Q_1, \dots, Q_n)$ sampled with time interval ε , so that Q_τ with $\tau = 1, \dots, n$ corresponds to the time point $t = \varepsilon\tau$. The continuous wavelet transform of Q is given by

$$W_s(\tau) = \frac{1}{\sqrt{s}} \sum_{\sigma=1}^n Q_\sigma \Gamma^* \left(\frac{\sigma - \tau}{s} \right) , \quad (\text{S2})$$

where the wavelet scale s is a dimensionless time scale. The inverse s^{-1} plays a similar role as the frequency in a Fourier transform. The so-called mother wavelet $\Gamma(u)$ is a complex oscillatory

function that quickly decays for large $|u|$ (23); Γ^* denotes its complex conjugate. Here we employ the Gabor wavelet function,

$$\Gamma(u) = \frac{e^{6iu} e^{-u^2/2}}{\pi^{1/4}}, \quad (\text{S3})$$

a complex plane wave damped by a Gaussian. The wavelet transform W_s is a complex function of s and τ that can be expressed in terms of its magnitude and phase,

$$W_s(\tau) = q_s(\tau) e^{i\varphi_s(\tau)}. \quad (\text{S4})$$

Note that the real part of Eq. (S4) is of the form of Eq. (S1), $\text{Re } W_s(\tau) = q_s(\tau) \cos \varphi_s(\tau)$, and φ_s can be interpreted as the phase of oscillation at the time scale associated with s (22). Hence, the wavelet scale s has to be chosen close to the characteristic period of oscillations of the time series Q . The resulting phase signal $\varphi_s(\tau)$ is however robust under small variations of the time scale s .

Phase maps

We use the wavelet transform to generate spatio-temporal maps of the phase (henceforth called “phase maps”) from intensity kymographs of the YFP signal along the PSM^{1,2}. To this end, we consider a time series of the intensity signal along a column of the intensity kymograph, $Q = (Q_1, \dots, Q_n)$, and apply the wavelet transform to obtain a phase time series $\varphi_s(\tau)$ (see Fig. 2B in the main text). Carrying out this procedure for every column c in the intensity kymograph yields a phase map $\varphi_s(c, \tau)$. Since the characteristic period of oscillations depends on the column c , we choose a wavelet scale $s(c)$ that is suitable for the respective column³. The time interval between rows in the kymograph is $\varepsilon = 5$ min and the spacing between columns is $\kappa = 1.26 \mu\text{m}$. Hence, we obtain a phase map $\varphi(x, t)$ that assigns a phase to every point in time $t = \varepsilon\tau$ and space $x = \kappa c$, using the wavelet scale $s(c)$. We choose $x = 0$ to correspond to the position of the posterior tip and $t = 0$ to the formation time of the 7th segment. The accuracy of the phase map $\varphi(x, t)$ can be evaluated by plotting the overlay of constant phase lines with the original intensity plot of the kymograph, showing very good agreement (example shown in Fig. S3).

For a fixed time t , the phase $\varphi(x)$ displays jumps from 2π to 0 (similar to Fig. 2B). We obtain a continuous phase signal $\phi(x)$ by removing these jumps, $\phi(x) = \mathcal{C}_x \varphi(x)$, where \mathcal{C}_x denotes the

¹We apply a Gaussian filter of radius 3 in spatial direction to the YFP intensity signal before carrying out the transform to enhance the coherence of the resulting phase map in the posterior.

²We used the *Mathematica* software package by *Wolfram Research, Inc.* to implement the wavelet transform.

³Wavelet scales are parameterized in an equal-tempered scheme, $s_{\mu\nu} = 2^{\mu-1+\nu/\bar{\nu}} T_G^{-1}$, where μ is called the octave number, ν the voice number, $\bar{\nu}$ is the number of voices per octave, and T_G is the so-called Fourier period of the Gabor wavelet function, Eq. (S3), $T_G = 4\pi/(6 + \sqrt{2 + 6^2})$ (23). We here choose $\mu = 4$ and $\bar{\nu} = 50$ for all columns. We choose the voice ν to depend on the column c , counted from the posterior, in the following way,

$$\nu(c) = \begin{cases} 5 & c \leq 100 \\ [(c-5)/20] & 100 < c \leq 400 \\ 20 & 400 < c \end{cases}, \quad (\text{S5})$$

where $[\cdot]$ denotes the nearest integer value. This yields $s(c) = 2^{3+\nu(c)/50} T_G^{-1}$.

removal of jumps in x -direction⁴. Carrying out this procedure for every time point t , we obtain a phase map $\phi(x, t) = \mathcal{C}_x\phi(x, t)$, which displays no jumps in x -direction (Supplementary Movie S4). In a similar way, we obtain a continuous signal of the posterior phase, $\phi_P(t) = \mathcal{C}_t\phi(0, t)$, where \mathcal{C}_t denotes the removal of jumps in t -direction.

We apply this procedure to the intensity kymographs of 18 embryos and thus obtain 18 phase maps, denoted by $\phi_i(x, t)$ with $i = 1, \dots, 18$, and the corresponding posterior phases $\phi_{P,i}(t)$. Furthermore, we determine the time-dependent PSM length $a_i(t)$ from the kymographs for each embryo.

Doppler effect and dynamic wavelength effect

Contributions to the frequency offset

The interplay of the decrease in PSM length with tissue level oscillations can be discussed by general theoretical arguments that are independent of any model, using the phase map $\phi(x, t)$. The values of the phase at the anterior end $x = a(t)$ and the posterior tip $x = 0$ are given by

$$\phi_A(t) = \phi(a(t), t), \quad (\text{S6})$$

$$\phi_P(t) = \phi(0, t), \quad (\text{S7})$$

where $a(t)$ is the length of the PSM at time t . The anterior and posterior periods T_A and T_P determined in Fig. 1E of the main text are related to these phases by $T_A = 2\pi/\omega_A$ and $T_P = 2\pi/\omega_P$, where

$$\omega_A = \frac{d\phi_A}{dt}, \quad (\text{S8})$$

$$\omega_P = \frac{d\phi_P}{dt}, \quad (\text{S9})$$

are the anterior and posterior angular frequencies.

The number of kinematic waves in the PSM as shown in Fig. 2D of the main text is given by the phase difference between anterior end and posterior tip as

$$K = \frac{\phi_P - \phi_A}{2\pi}. \quad (\text{S10})$$

Consequently, the rate of change of the number of kinematic waves is proportional to the offset between anterior and posterior frequency,

$$\frac{dK}{dt} = \frac{\omega_P - \omega_A}{2\pi} = \frac{1}{T_P} - \frac{1}{T_A}. \quad (\text{S11})$$

Thus, a decrease in the number of kinematic waves, $dK/dt < 0$, indicates that the anterior frequency is higher than the posterior frequency, $\omega_A > \omega_P$.

⁴We use an algorithm that first smoothes the signal using a moving median of width 5 in x -direction and then detects the phase jumps and eliminates them.

The frequencies ω_A and ω_P are connected in a kinematic relation that shows their dependence on the spatio-temporal features of the wave pattern. We use the definitions of the anterior and posterior phases, Eqs. (S6) and (S7), to write

$$\begin{aligned}\phi_A(t) &= \phi(a(t), t) \\ &= \phi_P(t) + \psi(a(t), t) .\end{aligned}\tag{S12}$$

where the phase profile ψ is defined by

$$\psi(x, t) = \phi(x, t) - \phi_P(t) .\tag{S13}$$

The phase profile would be time-independent if all phases along the PSM evolved with the same frequency. According to Eqs. (S8) and (S12), the anterior frequency is given by

$$\omega_A = \omega_P + \left(\frac{da}{dt} \frac{\partial \psi}{\partial x} + \frac{\partial \psi}{\partial t} \right) \Big|_{x=a(t)} ,\tag{S14}$$

where the derivatives of the phase profile $\partial \psi / \partial t$ and $\partial \psi / \partial x$ are evaluated at $x = a(t)$. Thus, the anterior frequency ω_A differs from the posterior frequency ω_P by the contributions from the phase profile,

$$\omega_D = \frac{da}{dt} \frac{\partial \psi}{\partial x} \Big|_{x=a(t)} ,\tag{S15}$$

$$\omega_W = \frac{\partial \psi}{\partial t} \Big|_{x=a(t)} .\tag{S16}$$

The contribution ω_D is caused by the change of PSM length and accounts for the effects of the anterior end moving towards the kinematic waves (Fig. 3A of the main text). It describes a Doppler effect in which da/dt is the speed of the moving observer, the anterior end, traveling into a wave with wavelength $2\pi / (\partial \psi / \partial x)$. The contribution ω_W is caused by the change of the phase profile ψ over time, which corresponds to a dynamic change of the kinematic wavelength (Fig. 3B of the main text). This contribution vanishes if oscillations at all positions x have the same period, since in this case $\partial \psi / \partial t = 0$.

In the section “Quantification of Doppler effect and dynamic wavelength effect in experiments”, we show that the two contributions ω_D and ω_W have opposite sign.

Discussion of simple scenarios

Eq. (S14) can be used to discuss the anterior and posterior frequencies in different simple scenarios:

Clock-and-wavefront scenario. In the original clock-and-wavefront scenario (20), the entire PSM oscillates homogeneously with a collective frequency Ω . The phase along the PSM is given by

$$\phi(x, t) = \Omega t ,\tag{S17}$$

and the phase profile is flat,

$$\psi(x, t) = 0 .\tag{S18}$$

Therefore, $\omega_W = 0$ and $\omega_D = 0$. According to Eq. (S14) there is no period offset, $\omega_A = \omega_P$. This is true even if the PSM changes its length, that is, if $da/dt \neq 0$.

Steady state PSM. In this case, the PSM has constant length $a(t) = a_0$, and displays a kinematic wave pattern that repeats with a collective frequency Ω , corresponding to a collective period of $T = 2\pi/\Omega$ (8, 9, 21). The phase $\phi(x, t)$ along the PSM is thus given by

$$\phi(x, t) = \Omega t + \psi(x) , \quad (\text{S19})$$

with a time-independent phase profile $\psi(x)$. In this case $\partial\psi/\partial t = 0$ and $da/dt = 0$, resulting in no period offset $\omega_A = \omega_P$, see Eq. (S14).

Scaling wave pattern. In this case, as the PSM shortens ($da/dt < 0$) it displays a kinematic wave pattern that scales with the length of the PSM (5). That is, the phase profile is a time independent function of the normalized PSM length. The phase $\phi(x, t)$ along the PSM is given by

$$\phi(x, t) = \omega_P t + \psi(x/a(t)) . \quad (\text{S20})$$

Accordingly, the phase profile is a function of $x/a(t)$ only. It is straightforward to check that in this case the contributions from the changing phase profile and the Doppler effect in Eq. (S14) exactly balance,

$$\omega_W = -\psi'(1) \frac{1}{a} \frac{da}{dt} , \quad (\text{S21})$$

$$\omega_D = +\psi'(1) \frac{1}{a} \frac{da}{dt} , \quad (\text{S22})$$

where ψ' denotes the derivative of ψ with respect to its argument. Consequently, the period offset is zero, $\omega_A = \omega_P$.

Quantification of Doppler effect and dynamic wavelength effect in experiments

By averaging experimental data from 18 embryos, we construct a phase map $\Phi(x, t)$ which represents the full spatio-temporal wave pattern during segmentation⁵. Similarly, we determine an average PSM length $A(t)$. Fig. S5 shows the phase map $\Phi(x, t)$ and the corresponding phase profile $\Psi(x, t) = \Phi(x, t) - \Phi(0, t)$ in a kymograph representation as in Fig. 2C of the main text.

We determine the anterior and posterior frequencies ω_A and ω_P from experimental data by evaluating Eqs. (S8) and (S9) for the average phase map $\Phi(x, t)$ and PSM length $A(t)$,

$$\omega_A(t) \approx \frac{d}{dt} \Phi(A(t), t) , \quad (\text{S23})$$

$$\omega_P(t) \approx \frac{\partial}{\partial t} \Phi(0, t) . \quad (\text{S24})$$

The frequencies ω_A and ω_P are displayed in Fig. S7A, which shows that the anterior frequency ω_A is larger than the posterior frequency ω_P over most of the time range. Furthermore, we estimate the contributions from the Doppler effect ω_D and the dynamic wavelength effect ω_W in experiments by evaluating Eqs. (S15) and (S16) for the average phase profile $\Psi(x, t)$ and PSM size $A(t)$,

$$\omega_D(t) \approx \left. \frac{dA}{dt} \frac{\partial \Psi}{\partial x} \right|_{x=A(t)} , \quad (\text{S25})$$

$$\omega_W(t) \approx \left. \frac{\partial \Psi}{\partial t} \right|_{x=A(t)} . \quad (\text{S26})$$

The results are shown in Fig. S7B. The Doppler contribution ω_D is positive (Fig. 3A of the main text), the dynamic wavelength contribution ω_W is negative (Fig. 3B of the main text). The combination of both contributions yields the observed frequency offset and is positive over most of the time range. Fig. S7C shows the relative offset between anterior and posterior frequency, $(\omega_A - \omega_P)/\omega_P$. Over most of the time range, the magnitude of the Doppler effect is larger than the dynamic wavelength effect (solid black curve). The average frequency offset over this time

⁵From the phase maps $\phi_i(x, t)$, we obtain phase profiles, $\theta_i(x, t) = \phi_i(x, t) - \phi_i(x_0, t)$ with $x_0 = 210 \mu\text{m}$ for each embryo $i = 1, \dots, 18$. We use the position $x_0 = 210 \mu\text{m}$ as subtraction point rather than $x = 0$ as in Eq. (S13), since the phase maps show the least degree of noise in this region. We then determine the median of θ_i at each x and t , $\bar{\theta}(x, t) = \text{median}_i \theta_i(x, t)$. The time evolution of the resulting median phase profile $\bar{\theta}$ is displayed in Supplementary Movie S5 (solid blue curve). As a smoothing technique, we perform fits of differentiable functions to the median phase profile $\bar{\theta}$ that capture its spatio-temporal key features. For a fixed time t , we fit the median phase profile $\bar{\theta}(x)$ with the function $\Theta(x)$ given in Table S1 using the fit parameters θ_0 , β , χ , and ξ . Carrying out this procedure for every time point, we obtain a time series for each of the fit parameters (blue curves in Fig. S8). We then calculate the phase profile $\Psi(x) = \Theta(x) - \Theta(0)$, which renders Ψ independent of the parameter θ_0 . We capture the time dependence of the remaining parameters β , χ , and ξ by fits of the functions $f_\beta(t)$, $f_\chi(t)$, and $f_\xi(t)$ given in Table S1. Using these fits in $\Psi(x)$, we obtain a differentiable function $\Psi(x, t)$ (dashed green line in Supplementary Movie S5). Likewise, we compute the median of the posterior phase $\bar{\phi}_P(t) = \text{median}_i \phi_{P,i}(t)$ and perform a fit of the function $\Phi_P(t)$ given in Table S1. According to Eq. (S13), the average phase map is thus given by $\Phi(x, t) = \Phi_P(t) + \Psi(x, t)$. Furthermore, we compute the mean PSM length of all embryos at each time point t , $\bar{a}(t) = \text{mean}_i a_i(t)$ and perform a fit with the function $A(t)$ given in Table S1. All fit results are shown in Fig. S8 (dashed black curves) and the resulting fit parameters are provided in Table S2. Note that all used fit functions are phenomenological and not derived from a dynamic theory.

interval is 8.4% (dashed black line). Note that a simple estimate of the offset between anterior and posterior frequency can also be determined through Fig. S5 using the argument presented in Fig. 3C of the main text. In Fig. S5A, we count ~ 11 posterior oscillations and ~ 12 anterior oscillations over the same range of time. Consequently, the average relative offset between anterior and posterior frequency can be estimated as $(12 - 11)/11 \approx 9\%$.

In Fig. S6, we show kymographs of the general spatial and temporal features of the wave patterns as obtained from experiments: (A) local inverse wavelength $\partial\Psi/\partial x$ of the average phase profile $\Psi(x, t)$, (B) rate of change of the phase profile $\partial\Psi/\partial t$, and (C) local frequency $\partial\Phi/\partial t$ of the average phase map $\Phi(x, t)$. Fig. S6A shows that the wave pattern exhibits long wavelengths (red) in the posterior and short wavelengths (blue) in the anterior. For a fixed position (column), the decrease of the wavelength over time is apparent (gradient from red to black to blue). Fig. S6B shows that the phase profile changes fastest in the anterior (green regions), where it yields the negative contribution ω_w , Eq. (S26). Fig. S6C reveals that different parts of the PSM are oscillating at different frequencies.

Supplementary Tables

Fit function	Fit parameters
$\Theta(x) = \theta_0 - \frac{\beta}{2} \left(x + \frac{1}{\chi} \log \cosh \chi(x - \xi) \right)$	$\theta_0, \beta, \chi, \xi$
$f_\beta(t) = \beta_0 + \beta_1 \tanh \beta_2(t - \beta_3)$	β_0, \dots, β_3
$f_\chi(t) = \chi_0 + \chi_1 \tanh \chi_2(t - \chi_3)$	χ_0, \dots, χ_3
$f_\xi(t) = \xi_0 + \frac{\xi_1}{2} \left(t + \frac{1 - \xi_2/\xi_1}{\xi_3} \log \cosh \xi_3(t - \xi_4) \right) - \frac{\xi_2}{2\xi_5} \log \cosh \xi_5(t - \xi_6)$	ξ_0, \dots, ξ_6
$\Phi_P(t) = \frac{p_0}{2}t + \frac{p_0}{2p_1} \left(\log \cosh p_1 p_2 - \log \cosh p_1(t - p_2) \right)$	p_0, \dots, p_2
$A(t) = a_0 + a_1 \tanh a_2(t - a_3)$	a_0, \dots, a_3

Table S1 Fit functions used in the Supplementary Text.

Parameter	Unit	Value
β_0	μm^{-1}	5.90024×10^{-2}
β_1	μm^{-1}	1.53338×10^{-2}
β_2	min^{-1}	1.53837×10^{-2}
β_3	min	2.8925×10^2
χ_0	μm^{-1}	1.20872×10^{-2}
χ_1	μm^{-1}	6.03996×10^{-3}
χ_2	min^{-1}	2.48799×10^{-2}
χ_3	min	2.0299×10^2
ξ_0	μm	1.89063×10^2
ξ_1	$\mu\text{m min}^{-1}$	-7.91625×10^{-1}
ξ_2	$\mu\text{m min}^{-1}$	2.54169×10^{-1}
ξ_3	min^{-1}	3.69293×10^{-2}
ξ_4	min	2.00622×10^2
ξ_5	min^{-1}	2.38447×10^{-2}
ξ_6	min	3.44444×10^2
p_0	min^{-1}	1.51274×10^{-1}
p_1	min^{-1}	5.28693×10^{-3}
p_2	min	6.40844×10^2
a_0	μm	4.17045×10^2
a_1	μm	2.02541×10^2
a_2	min^{-1}	-5.08818×10^{-3}
a_3	min	1.919×10^2

Table S2 Numerical values of the fit parameters of the functions given in Table S1.